

## FIRST VIEWS OF A NEARBY LIRG: STAR FORMATION AND MOLECULAR GAS IN IRAS 04296+2923

DAVID S. MEIER<sup>1,2</sup>, JEAN L. TURNER<sup>3</sup>, SARA C. BECK<sup>4</sup>, VAROUJAN GORJIAN<sup>5</sup>, CHAO-WEI TSAI<sup>3</sup>, AND SCHUYLER D. VAN DYK<sup>6</sup>

<sup>1</sup> Department of Physics, New Mexico Institute of Mining and Technology, 801 Leroy Place, Socorro, NM 87801, USA; [dmeier@nmt.edu](mailto:dmeier@nmt.edu)

<sup>2</sup> Adjunct Assistant Astronomer, National Radio Astronomy Observatory, P.O. Box O, Socorro, NM 87801, USA

<sup>3</sup> Department of Physics and Astronomy, UCLA, Los Angeles, CA 90095-1562, USA; [turner; cwtsai@astro.ucla.edu](mailto:turner@cwtsai@astro.ucla.edu)

<sup>4</sup> Department of Physics and Astronomy, Tel Aviv University, 69978 Ramat Aviv, Israel; [sara@wise.tau.ac.il](mailto:sara@wise.tau.ac.il)

<sup>5</sup> Jet Propulsion Laboratory, 4800 Oak Grove Boulevard, MS 169-327, Pasadena, CA 91109, USA; [varoujan.gorjian@jpl.nasa.gov](mailto:varoujan.gorjian@jpl.nasa.gov)

<sup>6</sup> Spitzer Science Center, California Institute of Technology, Mail Code 220-6, Pasadena, CA 91125, USA; [vandyk@ipac.caltech.edu](mailto:vandyk@ipac.caltech.edu)

Received 2008 December 18; accepted 2010 August 26; published 2010 October 13

### ABSTRACT

We present a first look at the local luminous infrared galaxy (LIRG) IRAS 04296+2923. This barred spiral galaxy, overlooked because of its location behind the Taurus molecular cloud, is among the half dozen closest ( $D = 29$  Mpc) LIRGs. More IR-luminous than either M82 or the Antennae, it may be the best local example of a nuclear starburst caused by bar-mediated secular evolution. We present Palomar J and Pa  $\beta$  images, Very Large Array continuum maps from  $\lambda = 20$ –1.3 cm, a subarcsecond Keck Long Wavelength Spectrometer image at  $11.7 \mu\text{m}$  and Owens Valley Millimeter Array CO(1–0),  $^{13}\text{CO}(1-0)$ , and 2.7 mm continuum images. The J-band image reveals a symmetric barred spiral galaxy. Two bright, compact mid-infrared and radio sources in the nucleus mark a starburst that is energetically equivalent to  $\sim 10^5$  O7 stars, separated by  $\lesssim 50$  pc. This is probably a pair of young super star clusters, with estimated stellar masses of  $\sim 10^7 M_{\odot}$  each. The nuclear starburst is forming stars at the rate of  $\sim 12 \pm 6 M_{\odot} \text{ yr}^{-1}$ , or about half of the total star formation rate for the galaxy of  $\sim 25 \pm 10 M_{\odot} \text{ yr}^{-1}$ . IRAS 04296+2923 is very bright in CO, and among the most gas-rich galaxies in the local universe. The  $^{12}\text{CO}$  luminosity of the inner half kpc is equivalent to that of the entire Milky Way. While the most intense CO emission is extended over a  $15''$  (2 kpc) diameter region, the nuclear starburst is confined to within  $1''$ – $2''$  (150–250 pc) of the dynamical center. Based on masses obtained with  $^{13}\text{CO}$ , we find that the CO conversion factor in the nucleus is lower than the Galactic value,  $X_{\text{CO}}^{\text{Gal}}$  by a factor of three to four, typical of gas-rich spiral nuclei. The nuclear star formation efficiency (SFE) is  $\tau_{\text{SF}}^{\text{nuc}} = \text{nuc} M_{\text{gas}} / \text{SFR}^{\text{nuc}} = 2.7 \times 10^{-8} \text{ yr}^{-1}$ , corresponding to a gas consumption timescale,  $\tau_{\text{SF}}^{\text{nuc}} \sim 4 \times 10^7$  yr. The SFE is 10 times lower in the disk, with  $\tau_{\text{SF}}^{\text{disk}} \sim 3.3 \times 10^8$  yr. The low absolute SFE in the disk implies that the molecular gas is not completely consumed before it drifts into the nucleus, and is capable of fueling a sustained nuclear starburst. IRAS 04296+2923 appears to be beginning a 100 Myr period as an LIRG, during which it will turn much of its  $6 \times 10^9 M_{\odot}$  of molecular gas into a nuclear cluster of stars.

**Key words:** galaxies: individual (IRAS 04296+2923, 2MASX J04324860+2929578) – galaxies: ISM – galaxies: starburst – radio continuum: galaxies

### 1. INTRODUCTION

Luminous ( $L_{\text{IR}} \gtrsim 10^{11} L_{\odot}$ ) and ultraluminous ( $L_{\text{IR}} \gtrsim 10^{12} L_{\odot}$ ) infrared galaxies are powered by prodigious amounts of star formation (Joseph & Wright 1985; Condon et al. 1991; Sanders & Mirabel 1996; Genzel et al. 1998; Lutz et al. 1998; Downes & Solomon 1998). While ultraluminous infrared galaxies (ULIRGs) are typically associated with mergers (Sanders et al. 1988), in luminous infrared galaxies (LIRGs), star formation may be generated by interactions or secular evolution, often related to bars (Kormendy & Kennicutt 2004). LIRGs are relatively rare (Soifer et al. 1987). The few LIRGs close enough for their internal structure to be resolved are valuable targets for the study of the local physics of the starburst/gas interaction, such as when and where the star formation takes place within a galaxy.

IRAS 04296+2923 (hereafter IRAS 04296) lies behind  $A_V \sim 5.5$  mag of extinction from the dark cloud L1500 in Taurus (Table 1). Low-resolution optical and H I spectra allowed it to be identified as a galaxy (Strauss et al. 1992; Chamaraux et al. 1995). IRAS 04296 has an IRAS luminosity of  $9.8 \times 10^{10} L_{\odot}$  (29 Mpc, for  $H_0 = 71 \text{ km s}^{-1} \text{ Mpc}^{-1}$ ; Sanders et al. 2003), making it the fifth most IR-luminous galaxy within 30 Mpc, at the lower bound of the LIRG class. It is 60% more IR-luminous than M82, and 35% more than the Antennae, exceeded only by NGC 1068, NGC 2146, NGC 7552, and NGC 1365 in the local universe.

Little is known about IRAS 04296. We discovered its nuclear starburst in a subarcsecond mid-infrared imaging survey with the Long Wavelength Spectrometer (LWS) on the Keck Telescope; it has a warm IRAS 60/100  $\mu\text{m}$  color that is a diagnostic of concentrated star formation. The bright double mid-IR source revealed by LWS (Section 3.1),  $\lesssim 1''$  (150 pc) across, suggested the presence of a new starburst galaxy in the local universe.

In this paper, we present near-infrared (NIR), mid-infrared (MIR), millimeter, and centimeter radio continuum images of IRAS 04296, as well as NIR and millimeter spectral imaging. While its location in Taurus hinders optical and ultraviolet observations of IRAS 04296, infrared and radio observations are unaffected, and they are the most reliable probes of star formation in dusty starbursts.

### 2. OBSERVATIONS

#### 2.1. Near-infrared J-band and Pa $\beta$ Images from the Hale Telescope

IRAS 04296 was observed using the Palomar Hale 5 m telescope<sup>7</sup> on 2005 January 23 UT with the Wide-field Infrared

<sup>7</sup> Based on observations obtained at the Hale Telescope, Palomar Observatory, as part of a continuing collaboration between the California Institute of Technology, NASA/JPL, and Cornell University.

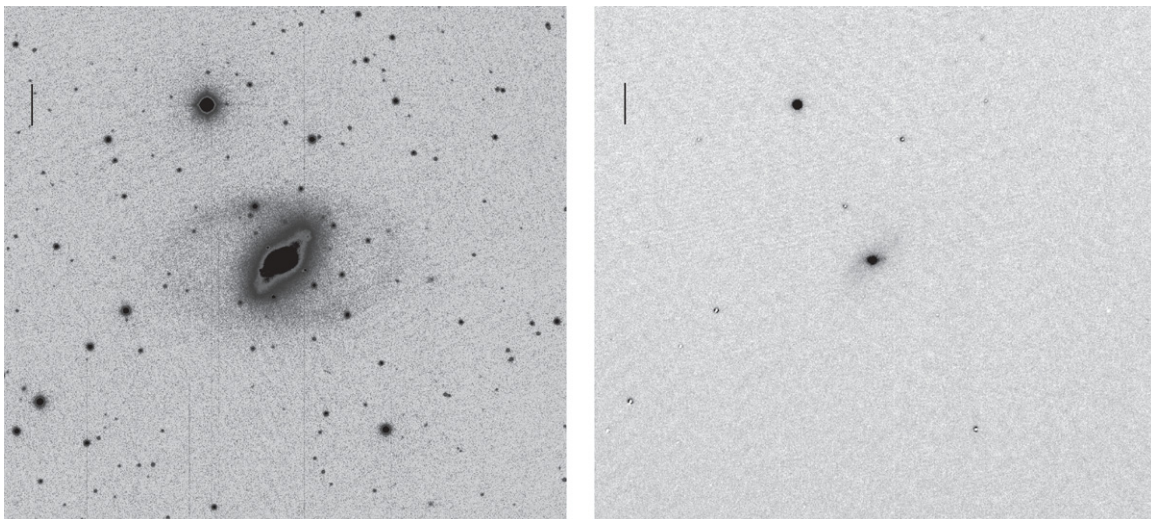


**Figure 1.** Left:  $J$ -band ( $1.25\ \mu\text{m}$ ) image of IRAS 04296 taken on the Palomar 5 m telescope. Right: Palomar continuum-subtracted  $\text{Pa}\ \beta$  image of IRAS 04296. The many point sources in the image are foreground Galactic stars of the Taurus region. Residuals from the continuum subtraction are seen in  $\text{Pa}\ \beta$ ; in particular, a large residual contribution remains from the bright foreground star to the northeast of the galaxy. These residuals are likely due to slight mismatches in the point-spread function of the (partially) saturated  $J$ -band stellar images. The scale bar is  $20''$  (2.8 kpc) in each plane. North is up and east is left.

**Table 1**  
IRAS 04296+2923 Basic Data

Characteristic	Value	Reference
Dynamical center <sup>a</sup> (kinematic)	$\alpha(2000) = 04^{\text{h}}32^{\text{m}}48^{\text{s}}:65 \pm 1''$ $\delta(2000) = +29^{\circ}29'57''.45 \pm 1''$	1
$2\ \mu\text{m}$ peak (2MASS)	$\alpha(2000) = 04^{\text{h}}32^{\text{m}}48^{\text{s}}:60 \pm 0''.3$ $\delta(2000) = +29^{\circ}29'57''.49 \pm 0''.3$	1
$V_{\text{lsr}}^{\text{a}}$	$2086\ \text{km s}^{-1}$	1
Adopted distance	29 Mpc	1
Position angle <sup>a</sup>	$252^{\circ}$	1
Inclination	$50^{\circ}$	1
$R_{\text{max}}(J\ \text{band})$	8.1 kpc	1
$R_{\text{max}}(\text{rotation curve})^{\text{a}}$	2.15 kpc	1
$v_{\text{max}}^{\text{a}}$	$190\ \text{km s}^{-1}$	1
$n^{\text{a}}$	1.25	1
$\theta_{\text{bar}}^{\text{b}}$	$-85^{\circ}$	1
$\Omega_{\text{bar}}^{\text{b}}$	$43\ \text{km s}^{-1}\ \text{kpc}^{-1}$	1
$M_{\text{H}_2}(<500\ \text{pc})^{\text{d}}$	$4.3 \times 10^8 M_{\odot}$	1
$\Sigma_{\text{H}_2}(<500\ \text{pc})^{\text{d}}$	$550 M_{\odot}\ \text{pc}^{-2}$	1
$M_{\text{dyn}}(<500\ \text{pc})^{\text{a}}$	$1.6 \times 10^9 M_{\odot}$	1
$M_{\text{H}_2}(<4.3\ \text{kpc})^{\text{c}}$	$5.9 \times 10^9 M_{\odot}$	1
$M_{\text{dyn}}(<30\ \text{kpc})^{\text{a}}$	$3.0 \times 10^{10} M_{\odot}$	1
$M_{\text{HI}}^{\text{tot}}$	$1.38 \times 10^9 M_{\odot}$	3
IRAS $12\ \mu\text{m}$ , $25\ \mu\text{m}$ , $60\ \mu\text{m}$ , $100\ \mu\text{m}$	1.39, 5.90, 42.1, 48.3 Jy	2
$L_{\text{IR}}$	$9.8 \times 10^{10} L_{\odot}$	2

#### Notes.

<sup>a</sup> Based on the best-fitting Brandt rotation curve (Section 3).

<sup>b</sup> Based on the best-fitting bar model (Figure 9).

<sup>c</sup> Assuming the standard CO conversion factor (Section 4.2).

<sup>d</sup> From  $^{13}\text{CO}(1-0)$  (Section 4.2).

**References.** (1) This paper; (2) Sanders et al. 2003; (3) Chamaraux et al. 1995.

Camera (WIRC; Wilson et al. 2003) at prime focus, in broadband  $J$  and narrowband  $\text{Pa}\ \beta$  filters. The camera has a pixel size of  $0''.25$ . Exposure times on source were 11 minutes ( $3 \times 20$  s frames, 11 pointings) for the continuum band and 18 minutes ( $3 \times 60$  s frames, 6 pointings) in the emission-line band, with equivalent off-source exposure times to measure the sky. The observing conditions were good with seeing at  $1''.0$  FWHM. Median dark current and filtered sky images created for each band were subtracted from the frames. Finally, a coadded mosaic

was produced from each set of on-source frames. We scaled the counts in each band's mosaic, via aperture photometry of several bright, uncrowded stars in the field around the galaxy, and subtracted the  $J$ -band mosaic (see Figure 1(a)) from the  $\text{Pa}\ \beta$  mosaic, to produce an approximate continuum-subtracted image (see Figure 1(b)). The images in the broadband and narrowband filters were not explicitly flux calibrated using observations of standard stars, so we are unable to derive a value for the net  $\text{Pa}\ \beta$  flux in the continuum-subtracted image.

## 2.2. Mid-infrared Images from Keck

IRAS 04296 was observed on 2002 December 24 with the LWS in imaging mode on the Keck I Telescope, with the standard  $11.7\ \mu\text{m}/\text{SIC}$  filter. The standard stars were  $\alpha$  Aur,  $\alpha$  Aries, and  $\beta$  Leo, observed both before and after the source exposures. High quality images at both wavelengths were obtained (Figure 2); however, the absolute flux calibration was uncertain due to intermittent instrumental problems, and so we reobserved the galaxy on January 31, with the same parameters as confirmation. Absolute flux calibration is estimated to be good to 10%, based on derived flux counts on standard star before/after observations throughout the night. Stellar images were about 5 pixels or  $0''.4$  FWHM.

## 2.3. Radio Continuum Images from the VLA

The radio data were taken with the NRAO VLA.<sup>8</sup> There were two projects: AB1092 on 2003 July 7 with the A configuration for high angular resolution at  $\lambda = 20\ \text{cm}$ , 6 cm, 3.5 cm, 2 cm, and 1.3 cm ( $L$ ,  $C$ ,  $X$ ,  $U$ , and  $K$  bands) and AT309 on 2005 July 5 with the array in BC configuration for moderate resolution at 1.3 cm only. 3C48 was the primary calibrator for both runs. The 20, 6, and 3.6 cm data were processed with AIPS, including baseline corrections. The 2 cm and 1.3 cm data were observed in fast-switching mode and reduced according to the AIPS prescriptions

<sup>8</sup> The National Radio Astronomy Observatory is a facility of the National Science Foundation operated under cooperative agreement by Associated Universities, Inc.

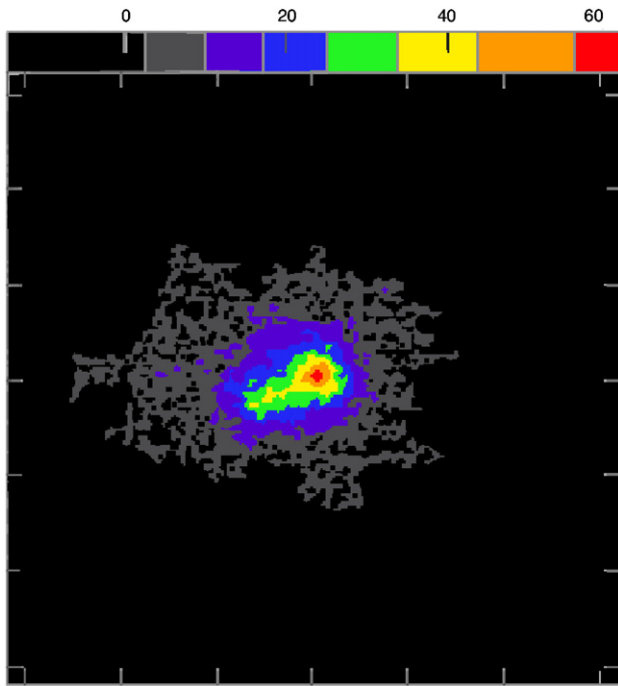


**Figure 2.** LWS image of IRAS 04296 at  $11.7\mu\text{m}$ . The scale in counts  $\text{pixel}^{-1}$  is above the figure and the conversion is  $4.1 \times 10^{-5} \text{ Jy count}^{-1}$  for a 360 s integration. North is up and east is left.

for high frequency calibration. The details of the radio imaging are discussed below (Section 3.2).

#### 2.4. Millimeter CO Lines and Continuum from OVRO

Simultaneous aperture synthesis observations of the  $^{12}\text{CO}(1-0)$  transition (115.271 GHz) and the  $^{13}\text{CO}(1-0)$  transition (110.201 GHz) of IRAS 04296 were made with the Owens Valley Radio Observatory (OVRO) Millimeter Interferometer between 2003 November 1 and 2004 May 8. The interferometer consisted of six 10.4 m antennas with cryogenically cooled SIS receivers (Scoville et al. 1994). Observations in “Compact,” “Low,” and “High” configuration were obtained, with system temperatures (single sideband) ranging from 220 to 450 K at 115 GHz.  $64 \times 4$  MHz channels were used to cover both transitions, giving a velocity resolution of  $10.5 \text{ km s}^{-1}$  for  $\text{CO}(1-0)$ . The phase center is within  $0''.5$  of the  $2\mu\text{m}$  peak listed in Table 1 and the adopted systemic velocity (LSR) was  $2100 \text{ km s}^{-1}$ . Simultaneous low spectral resolution, wideband ( $128 \times 31.25$  MHz) COBRA observations were used to generate a 3 mm continuum image ( $\nu_o \simeq 111$  GHz), free from  $^{12}\text{CO}(1-0)$ ,  $\text{CN}(1-0)$ , and  $^{13}\text{CO}(1-0)$  contamination. The data were calibrated using the MMA software package. Phase calibration was done by observing the quasar J0336+323 every 25 minutes. Absolute flux calibration was done using Uranus as the primary flux calibrator and 3C273 and 3c454.3 as secondary flux calibration, and is good to  $\sim 10\%$ .

Mapmaking was done in MIRIAD and subsequent data analysis and manipulation was done with the NRAO AIPS package. Maps were generated with natural weighting to maximize sensitivity, uniform weighting to maximize resolution and robust = 0 weighting to simultaneously optimize sensitivity and resolution. Unless stated the analysis results from the naturally weighted data. Integrated intensity images are straight moment 0 maps with all emission brighter than  $1.3\sigma$  ( $1\sigma$  for  $^{13}\text{CO}$ ) per channel included. The OVRO primary beam is  $\sim 64''$  at 115 GHz. Correc-

tions for the primary beam have not been applied so emission at the edge of the primary beam will be somewhat underestimated. Structures extended on scales larger than  $\sim 52''$  for  $\text{CO}(1-0)$  will be resolved out by the interferometer. No single-dish observations of this galaxy exists, so no estimate of the amount of resolved-out flux is possible for the millimeter-wave images. However,  $52''$  corresponds to spatial scales of 7.3 kpc and given that the emission must be extended on this scale in an individual channel to be missed, we consider it unlikely that significant flux is resolved out. If large amounts of flux are missed then the observed molecular richness is a lower limit.

### 3. RESULTS: A FIRST LOOK AT IRAS 04296+2923

Near-infrared images of IRAS 04296 reveal a normal, barred spiral galaxy in starlight. The bright, concentrated nuclear starburst is prominent at MIR and radio continuum wavelengths. In Section 3.1, we discuss the large field Palomar near-IR images of the galaxy and its Pa  $\beta$  emission, and the Keck high-resolution  $11.7\mu\text{m}$  MIR image. In Section 3.2, we discuss the VLA radio images, which were mapped in four ways, one to match beams for extended emission dominated by synchrotron emission, and three for matching compact emission dominated by free-free from H II regions. In Section 3.3, we discuss the CO and molecular gas.

#### 3.1. Infrared Views

The Palomar *J*-band continuum image and a narrowband continuum-subtracted image of Pa  $\beta$  in IRAS 04296 are shown in Figure 1. The near-infrared continuum at *J* band reveals the stellar population. IRAS 04296 is an inclined, barred spiral with outer ring-like spiral arms (SBb/c(r)). The total extent of the emission is roughly  $2-2.5$ , or  $17-20$  kpc ( $8-10$  kpc in radius). The stellar distribution appears bi-symmetric and undistorted. The Pa  $\beta$  image shows line emission to be very concentrated and bright in the galactic nucleus, with some very weak emission along the inner arms. The compact nature of the bright Pa  $\beta$  emission shows that the starburst is highly concentrated at the nucleus. Since the images are not photometric, and extinction is probably variable across the galaxy, we cannot precisely quantify the relative brightnesses of disk and nuclear star formation from the Pa  $\beta$  image.

Mid-IR continuum emission traces warm ( $\sim$  few hundred K) dust heated by young stars in the starburst. The high-resolution ( $0''.3$ ) mid-IR continuum image at  $11.7\mu\text{m}$  made with LWS on Keck of IRAS 04296 is shown in Figure 2; the field of view of this image is only  $10'' \times 10''$ , or about 1.4 kpc on a side. A similar  $18.75\mu\text{m}$  image (not shown) will be published in a subsequent paper (J. L. Turner et al. 2010, in preparation). The  $11.7\mu\text{m}$  filter contains two polycyclic aromatic hydrocarbon (PAH) features; however, based on observations of the starburst galaxies NGC 7714 and Arp 220 (Brandl et al. 2004; Armus et al. 2007) we estimate that at most 15% of the  $12\mu\text{m}$  continuum is due to PAH emission.

The mid-IR emission comprises a bright source, which cannot be resolved at the  $0''.3$  diffraction limit of Keck at  $11.7\mu\text{m}$ , and a secondary source or tail extending to the east of the main source, separated from the main source by  $\sim 1''.5$  ( $\sim 200$  pc). The total flux density is  $S_{11.7\mu\text{m}} = 680 \text{ mJy}$ . These two compact, mid-infrared sources account for roughly half of the IRAS  $12\mu\text{m}$  flux of the entire galaxy.

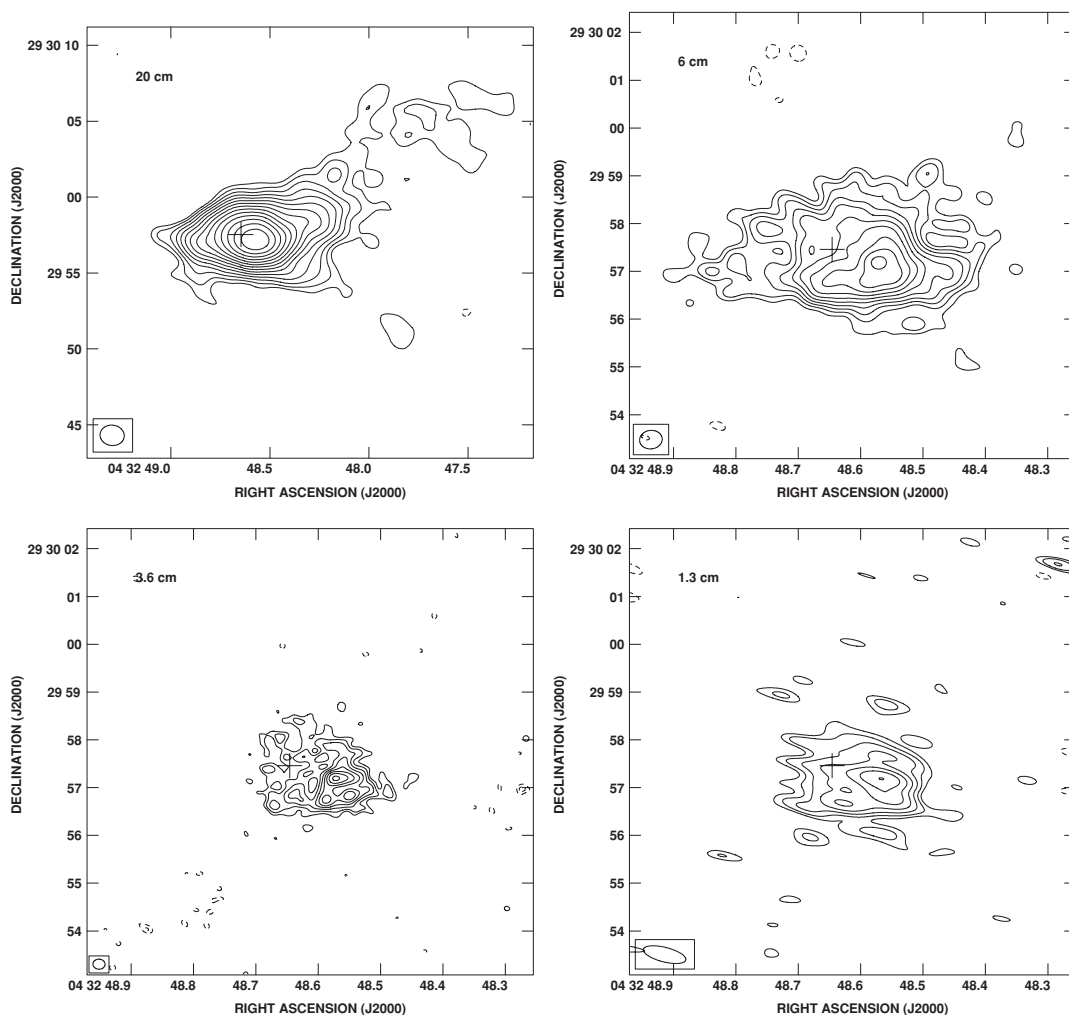


**Figure 3.** Maps of the radio continuum, emphasizing extended emission. Top left: 20 cm; top right: 6 cm; bottom left: 3.6 cm; bottom right: 1.3 cm with the BC array. Contour intervals are  $\pm 2^{n/2}$  ( $3\sigma$ ) of the following increments: 0.25 mJy, 0.15 mJy, 0.12 mJy, and 0.25 mJy beam $^{-1}$  for 20, 6, 3.6, and 1.3 cm, respectively. The dynamical center is displayed in the 20 cm and 6 cm maps.

**Table 2**  
Infrared and Radio Fluxes

$\lambda$	rms (mJy beam $^{-1}$ )	Beam (Robust = 0) ("x", p.a. $^\circ$ )	$\theta_{\max}$ "	Peak Flux (mJy beam $^{-1}$ )	Total Mapped <sup>a, b</sup> (mJy)	Cut Flux <sup>b, c</sup> ( $u, v$ ) <sub>min</sub> = 18k $\lambda$ (mJy)	Cut Flux <sup>b, c</sup> ( $u, v$ ) <sub>min</sub> = 50k $\lambda$ mJy
20 cm	0.11	1.60 $\times$ 1.35, 82.8	38	32	130 $\pm$ 10	71 $\pm$ 5	...
6 cm	0.04	0.48 $\times$ 0.39, -83.3	10	3.8	59 $\pm$ 5	28 $\pm$ 3	...
3.6 cm	0.034	0.25 $\times$ 0.21, 88.2	7	1.5	25 $\pm$ 5	14 $\pm$ 2	11 $\pm$ 2
2 cm	0.085	0.18 $\times$ 0.138, -53.9	4	1.0	10 $\pm$ 1	...	10 $\pm$ 2
1.3 cm	0.068	0.1 $\times$ 0.09, -80.39	2	0.5	7 $\pm$ 1.5	...	7 $\pm$ 1.5
1.3 cm BC array	0.16	0.91 $\times$ 0.30, 76	20	3.7	23 $\pm$ 5	18 $\pm$ 3	...
2.7 mm	0.75	4.6 $\times$ 3.8, 8	52	9.9	11 $\pm$ 2	...	...
11.7 $\mu$ m	5.1 counts s $^{-1}$	0.4	n.a.	71 $\pm$ 10	680 $\pm$ 100	...	...

**Notes.**

<sup>a</sup> Based on “uncut” maps with full native A configuration ( $u, v$ ) coverage.

<sup>b</sup> Quoted uncertainties in the fluxes are based on three times the rms times  $\sqrt{N}$  times the number of beams corresponding to the source size; they do not include resolved-out flux, or the estimated 5% (10% at 2 and 1.3 cm) absolute flux scale uncertainty. Large beam fluxes do not exist for wavelengths other than 20 cm, so we cannot estimate amounts of resolved-out flux except at 20 cm, where it is negligible. Fluxes are measured within  $\lambda/B_{\min}$  for each map.

<sup>c</sup> Based on “cut” maps restricted in ( $u, v$ ) coverage. The 18 k $\lambda$  fluxes correspond to the maps of Figure 3, and the 50 k $\lambda$  fluxes to those of Figures 5 and 6. See Section 3.2.

### 3.2. Radio Views

VLA maps of IRAS 04296 across the centimeter waveband are presented in Figure 3, with fluxes and noise values given

in Table 2. The radio continuum emission is a combination of thermal bremsstrahlung emission from the H II regions and non-thermal synchrotron emission from supernovae and their remnants associated with the starburst. The brightest radio

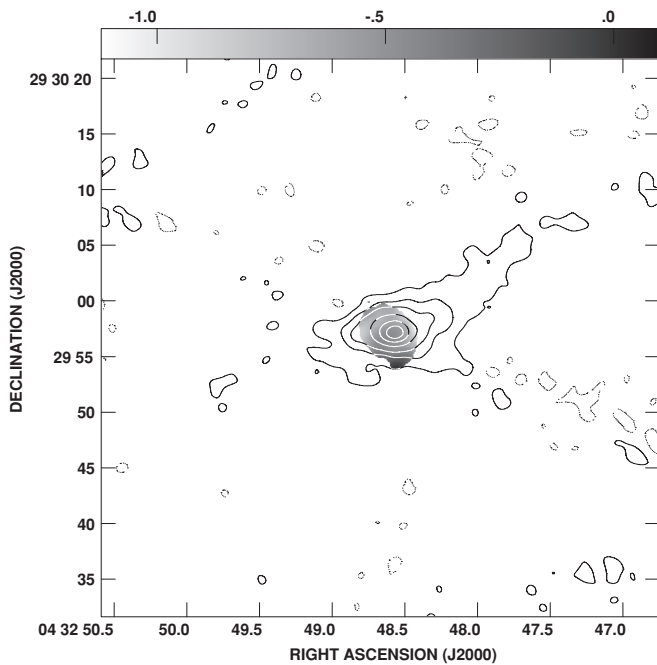


**Figure 4.** Spectral index between 1.3 and 20 cm in gray scale, overlaid with representative contours of the 20 cm emission. The spectral index is not uniform over the whole frequency range covered, but maps at other frequencies appear similar to this.

emission, like the mid-IR emission, is concentrated within the central  $1''$ – $2''$  region of  $\sim 150$ – $250$  pc extent; higher resolution maps shown below give a better comparison with the Keck mid-IR images.

Separating free-free emission from the H II regions from the synchrotron emission is possible because these sources have different spectral and spatial characteristics. However, complications arise when comparing aperture synthesis maps at different frequencies, so the spectral analysis must be done with care. The synchrotron component in galaxies is spatially extended with a spectrum that falls steeply with increasing frequency. Free-free emission from H II regions is compact with spectra that are either flat or rising with frequency (e.g., Turner & Ho 1994). Except at 1.3 cm, the robustly weighted VLA maps of Figure 3 were done with a single array configuration, so the maps have responses to extended structure that vary with frequency; shorter wavelength maps are less sensitive to extended emission. The shortest baselines determine the maximum detectable spatial scales,  $\theta_{\max} \sim \lambda/B_{\min}$ , which are listed in Table 2. So the maps of Figure 3 cannot be compared directly to obtain spectral index maps. Since single dish or lower resolution VLA fluxes do not exist for IRAS 04296 except at 20 cm, we cannot estimate the effects of missing short baselines except at 20 cm. Our A array maps, with total flux  $S_{20\text{ cm}} = 140 \pm 7$  mJy, recover the entire 20 cm flux recorded by Condon et al. (1996), and so the 20 cm map is probably a good representation of the total radio emission, although there may be faint extended emission that is undersampled. From the 20 cm image we can see that the extended radio emission is aligned along the apparent bar of the galaxy (Section 3.3). The bright mid-IR sources and the peak of the radio emission mark a starburst located at the inner end of the northwestern arm traced by CO (Section 3.3).

Free-free and non-thermal synchrotron sources can be separated by determining the spectral index,  $\alpha$ , of the emission

( $S \propto \nu^\alpha$ ) so long as the beams are matched, not only in beam size ( $\theta_{\min}$ ), but also in  $\theta_{\max}$ , defined by  $u_{\min} = B_{\min}^{\text{EW}}/\lambda$ ,  $v_{\min} = B_{\min}^{\text{NS}}/\lambda$ . Toward this end we have made a series of “cut” maps, which are high-pass spatially filtered images with common  $\theta_{\min}$  and  $\theta_{\max}$ , that enable us to construct images with nearly identical  $(u, v)$  coverages and allow us to compare the radio spectra for the compact sources, at the cost of losing response to extended emission. Since the star formation arises largely in compact sources  $\lesssim 1''$  (150 pc), we expect to detect nearly all of the free-free emission in the “cut” maps and resolve out most of the synchrotron emission, which is our goal.

The first set of “cut” maps were made to match the beams at 20, 6, 3.6, and 1.3 cm, with a consistent  $(u, v)_{\min}$  of  $18\text{ k}\lambda$  ( $\theta_{\max} \sim 10''$ ; 1.4 kpc). The beam for this series of maps is  $0'.82 \times 0'.29$ , position angle (p.a.  $-89^\circ$ ). For the 1.3 cm emission, we used the BC configuration data. From the cut maps, we mapped the spectral index  $\alpha$ , shown in Figure 4. The spectral index is negative over the entire range, confirming that the extended emission centimeter-wave emission is largely non-thermal, typical of large spiral galaxies and LIRGs (e.g., Condon et al. 1991; Condon 1992; Clemens et al. 2008). Fluxes from this set of maps are measured for a  $4'.5 \times 3''$  box (630 pc  $\times$  420 pc) and are shown in Table 2.

A second set of “cut” maps were made from the shorter wavelength data to image the compact emission at 3.6, 2, and 1.3 cm. For these maps,  $(u, v)_{\min} = 50\text{ k}\lambda$  ( $\theta_{\max} \sim 4''$ , or  $\sim 550$  pc) and they were convolved to match the  $0'.27 \times 0'.23$ , p.a.  $-90^\circ$  beam ( $\theta_{\min}$ ) of the 3.6 cm map. These cut maps are shown in Figure 5, and fluxes are given in Table 2. The peak flux densities are the same within observational uncertainties for all three maps,  $1.1$ – $1.5$  mJy beam $^{-1}$ . The  $(u, v)$  restriction has eliminated about two-thirds of the total 3.6 cm flux as compared to the map of Figure 3. The compact emission that remains in these maps has a nearly flat spectrum: this is emission from H II regions. These radio images are similar to the  $11.7\ \mu\text{m}$  image of Figure 2, given the lower resolution ( $0'.3$ ) of the mid-IR image. We identify the brightest, elongated radio source with the mid-IR peak, and the extension visible to the southeast in the 3.6 cm image (Figure 5) with the extension in the mid-IR image.

A third set of “cut” maps, designed to match beams at 2 and 1.3 cm, gives the highest resolution images. Like the previous set of maps, they are cut to  $(u, v)_{\min} = 50\text{ k}\lambda$ , but these maps are instead convolved to match the smaller 2 cm beam of  $0'.15 \times 0'.14$ , p.a.  $-66^\circ$ . These images resolve the brightest continuum source (Figure 6) into a double source separated by  $0'.2$ , or 30 pc oriented east–west. The eastern source is stronger. Slight differences in the spatial structure of the double source at the two frequencies might be due to differences in azimuthal  $(u, v)$  coverage or to 1.3 cm seeing. This source is flat in radio spectral index, indicating that the compact emission is largely free-free emission from H II regions. Comparison of the three sets of maps suggests that the total amount of flat spectrum, compact emission in the nucleus of IRAS 04296 is  $\sim 10$  mJy.

Continuum emission at 2.7 mm was detected with OVRO (Figure 7d). The peak 2.7 mm continuum intensity is  $10 \pm 1$  mJy beam $^{-1}$  ( $4'.6 \times 3'.7$ ) with a total detected flux of  $11 \pm 2$  mJy (Table 2). The millimeter continuum emission is confined to the nuclear starburst, with position and extent consistent with the (uncut) centimeter-wave and infrared continuum. At this wavelength, potential continuum sources include synchrotron, free-free emission, and dust. Extrapolation of synchrotron emission all the way from 20 cm to 2.7 mm is dangerous since it is sensitive to the exact spectral index, but using the 20 cm

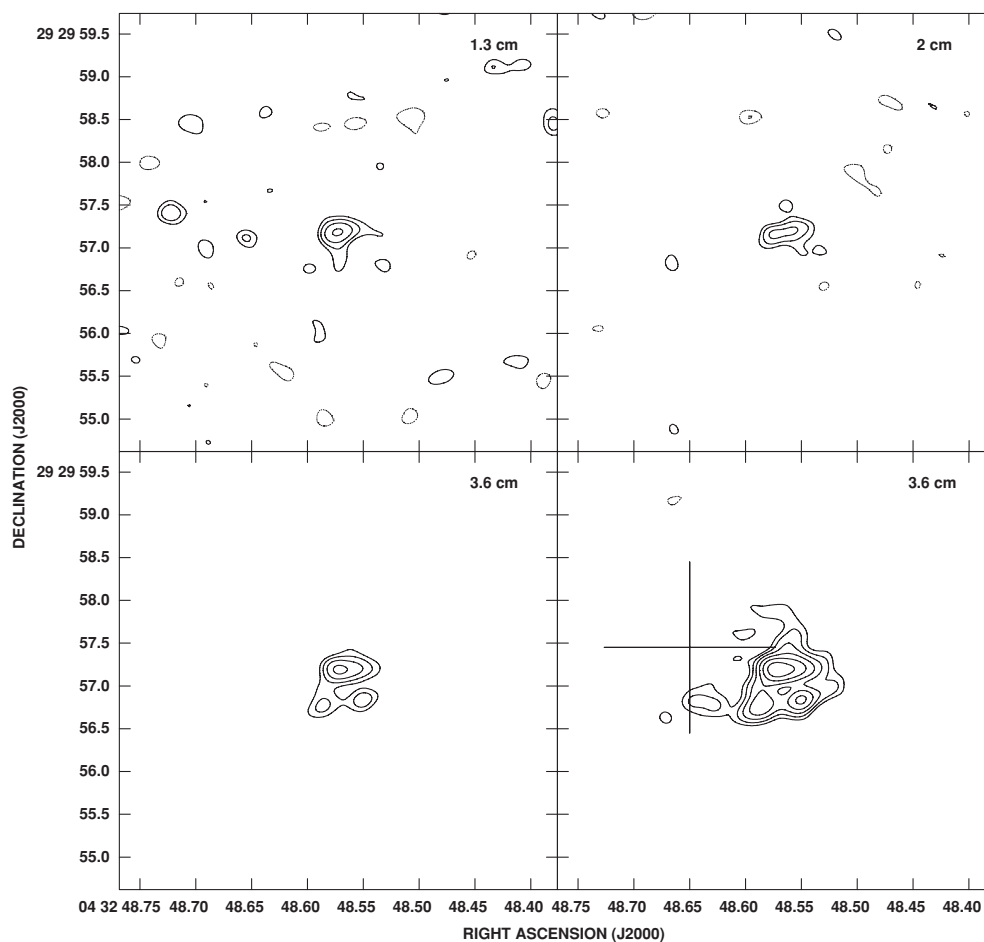


**Figure 5.** Matching 3.6, 2, and 1.3 cm continuum images of IRAS 04296 made from “cut” data as described in the text, with consistent  $(u, v)$  coverage and a beam size of  $0''.15 \times 0''.14$ , p.a.  $-66^\circ$ . The bright central source, elongated east–west with a size of  $\sim 0''.5$  has a flat spectrum, containing flux  $\sim 3$  mJy. The central arcsecond contains  $\sim 6$  mJy at 1.3 cm. Contours are  $\pm 2^{0.5i} \times 0.5$  mJy beam $^{-1}$  ( $\sim 2.5\sigma$ – $3\sigma$  at 2 and 1.3 cm). The 3.6 cm maps are most affected by the cut of short  $(u, v)$  spacings. (a) Top left: 1.3 cm. Peak flux is  $1.5$  mJy beam $^{-1}$ , total flux 7 mJy. (b) Top right: 2 cm. Peak flux is  $1.1$  mJy beam $^{-1}$ , total flux 10 mJy. (c) Bottom left: 3.6 cm. Peak flux is  $1.6$  mJy beam $^{-1}$ , total flux 10–11 mJy. (d) Bottom right: 3.6 cm map as in (c), except plotted with a lowest contour of  $0.2$  mJy beam $^{-1}$ . Cross marks the location of the dynamical center from the CO maps.

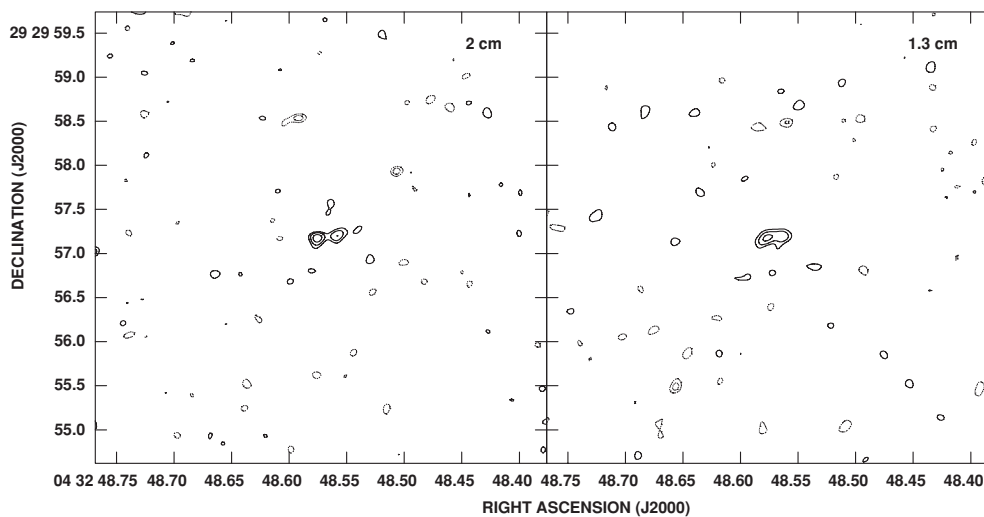


**Figure 6.** Matching 2 and 1.3 cm continuum images of IRAS 04296. Contours are  $\pm 2^{0.5i} \times 0.35$  mJy beam $^{-1}$  ( $2.5\sigma$ ). Beam for both maps is  $0''.15 \times 0''.14$ , p.a.  $-66^\circ$ . Left: 2 cm image, with  $(u, v)$  coverage cut to match the 1.3 cm image as described in the text. Peak flux is  $0.9$  mJy beam $^{-1}$ . Right: 1.3 cm map convolved to the same beam as the 2 cm image in (a). Peak flux is  $0.8$  mJy beam $^{-1}$ .

emission seen in the first “cut” map and  $\alpha = -0.8$  implies a contribution of 2–3 mJy. Based on our estimated nuclear gas mass (Section 4.2) we expect that  $\sim 1$ –2 mJy of the 3 mm

continuum is from dust emission. From this, we conclude that the millimeter continuum flux associated with star formation is  $\gtrsim 5$ –7 mJy at 2.7 mm, consistent with the fraction of the

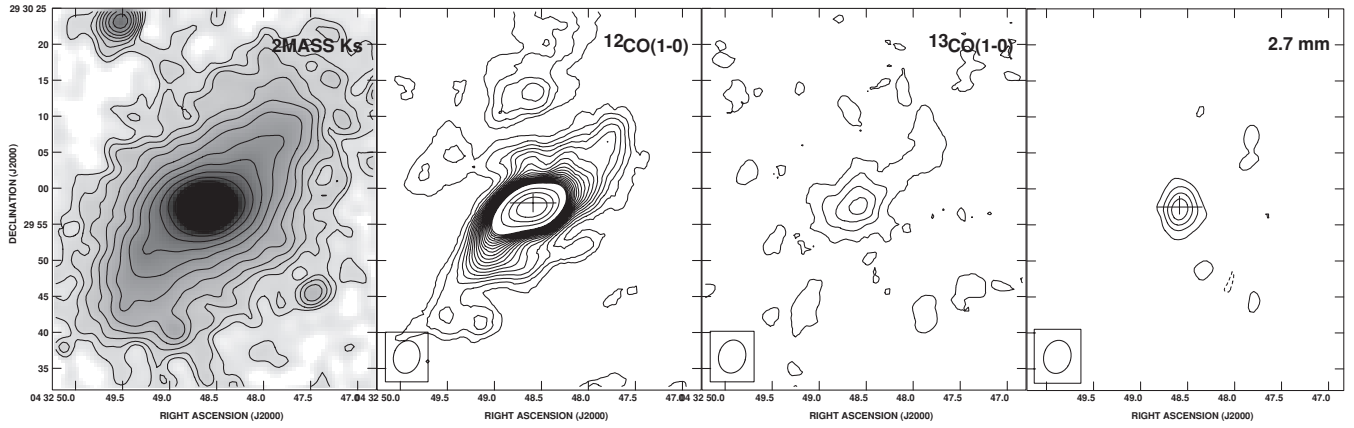


**Figure 7.** Far left: 2MASS  $K_s$  image of IRAS 04296 over the same region covered by the molecular data. Contours are logarithmic in arbitrary units. Middle left: the naturally weighted  $^{12}\text{CO}(1-0)$  intensity map. Contours are  $13.9 \text{ K km s}^{-1} \times 1, 2, 3, \dots, 20, 30, 40, 50$  for a beam size of  $4''.6 \times 3''.6; -14^\circ$ . Middle right: the  $^{13}\text{CO}(1-0)$  integrated intensity map of IRAS 04296 displayed at the same resolution as  $^{12}\text{CO}(1-0)$ . Contours are in steps of  $10.3 \text{ K km s}^{-1}$ . Far right: the 2.7 mm continuum map generated from the line-free channels of the wideband data set. Contours are in steps of  $2.0 \text{ mJy beam}^{-1}$  ( $2\sigma$ ) for a beam size of  $4''.6 \times 3''.8; -15^\circ$ . The crosses in the middle planes mark the location and extent of the 6 cm radio continuum emission.

flux from the compact flat-spectrum sources seen directly in centimeter-wave continuum.

### 3.3. Molecular Views

The first observations of molecular gas toward IRAS 04296 are shown in Figures 7 and 8. The  $\text{CO}(1-0)$  integrated intensity (Figure 7) is remarkably bright, extending over a 2.5 kpc (diameter) region, peaking at the nucleus. (When no superscript appears the most abundant from  $^{12}\text{C}^{16}\text{O}$  is implied; “ $^{13}\text{CO}$ ” refers to the less abundant  $^{13}\text{C}$  substituted isotopologue.) The CO emission extends well beyond the Pa  $\beta$  emission region (Figure 1(b)) and the radio continuum (Figure 8). Beyond the nucleus the molecular gas is bar-like, extended southeast–northwest. Weak emission is also seen to the north and west of the nucleus. The CO morphology closely follows the stellar morphology seen in the Palomar  $J$ -band and Two Micron All Sky Survey (2MASS)  $K_s$  images, as shown in Figure 7.

Toward the nucleus, antenna temperatures in the robustly weighted image (Figure 8) peak at 10 K averaged over the inner 160 pc radius. This is a remarkably high brightness temperature for a galaxy at the distance of IRAS 04296; it implies that the beam filling factor for the CO must be near unity over regions 300–400 pc in diameter. The CO line widths are broadest toward the nucleus but are fairly modest ( $250 \text{ km s}^{-1}$ ; FWHM) compared to other luminous starbursts (Solomon et al. 1992, 1997; Downes & Solomon 1998), and drop to  $\sim 50 \text{ km s}^{-1}$  toward the outer molecular arms. The velocity field is consistent with a rotating disk, except for modest perturbations ( $\lesssim 50 \text{ km s}^{-1}$ ; see below). We have fit the axisymmetric velocity field with a Brandt rotation curve; the best-fit parameters are given in Table 1. The separate CO component north of the nucleus follows the same velocity field as does the bar and nucleus. This suggests that these clouds are a continuation of the galaxy’s disk (the outer spiral arms).

The molecular morphology is bar-like. The best fit for the kinematic major axis from the CO velocity field is at a position angle of  $252^\circ$  (to the receding axis). This is perpendicular to the long axis of the CO and IR morphology. Therefore, the observed bar-like structure seen in CO is not a result of inclination, but is intrinsic. The strong bar deduced for the stellar distribution makes it impossible to separately constrain the bar strength and the galaxy’s inclination angle,  $i$ , over the inner arcminute.

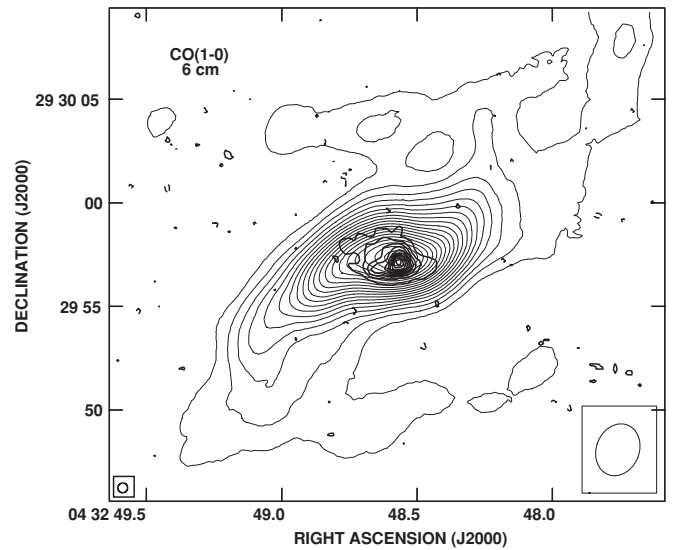


**Figure 8.** 6 cm radio continuum (bold lines) overlaid on the central region of the robustly weighted  $\text{CO}(1-0)$  image (thin lines).  $\text{CO}(1-0)$  contours are in steps of  $4 \text{ Jy beam}^{-1} \text{ km s}^{-1}$ , while the 6 cm contours are  $0.2 \text{ mJy beam}^{-1} \times -3, -1, 1, 3, 5, \dots$ . The 6 cm beam is in the lower left and the  $\text{CO}(1-0)$  beam ( $2''.6 \times 2''.1; 21^\circ 6'$ ) is in the lower right.

Instead we estimate the inclination angle from the axial ratio of the outer, presumably more circular, spiral arms seen in the  $J$ -band image (Figure 1(a)). The measurement yields  $i = 50 \pm 4^\circ$  and is consistent with the same p.a. determined from the CO velocity field. Such an inclination angle implies a peak velocity of  $\sim 190 \text{ km s}^{-1}$ , or a dynamical mass of  $1.6 \times 10^9 M_\odot$  over the  $7''$  ( $R < 500 \text{ pc}$ ) and  $3 \times 10^{10} M_\odot$  over the radius,  $R = 30''$  ( $R < 4.3 \text{ kpc}$ ). This suggests that IRAS 04296 is similar in size to the Milky Way at this radius. H I observations at larger radii will be needed to determine a global dynamical mass for IRAS 04296.

To verify that the gas distribution and kinematics are consistent with response to a bar potential, we generate a simple analytical, weak-bar model. These models treat the gas dissipation by adding a damping term proportional to radial velocity to the standard stellar barred orbits (e.g., Wada 1994; Lindblad & Lindblad 1994). Despite the simplicity of the model, it matches full hydrodynamical simulations with surprising

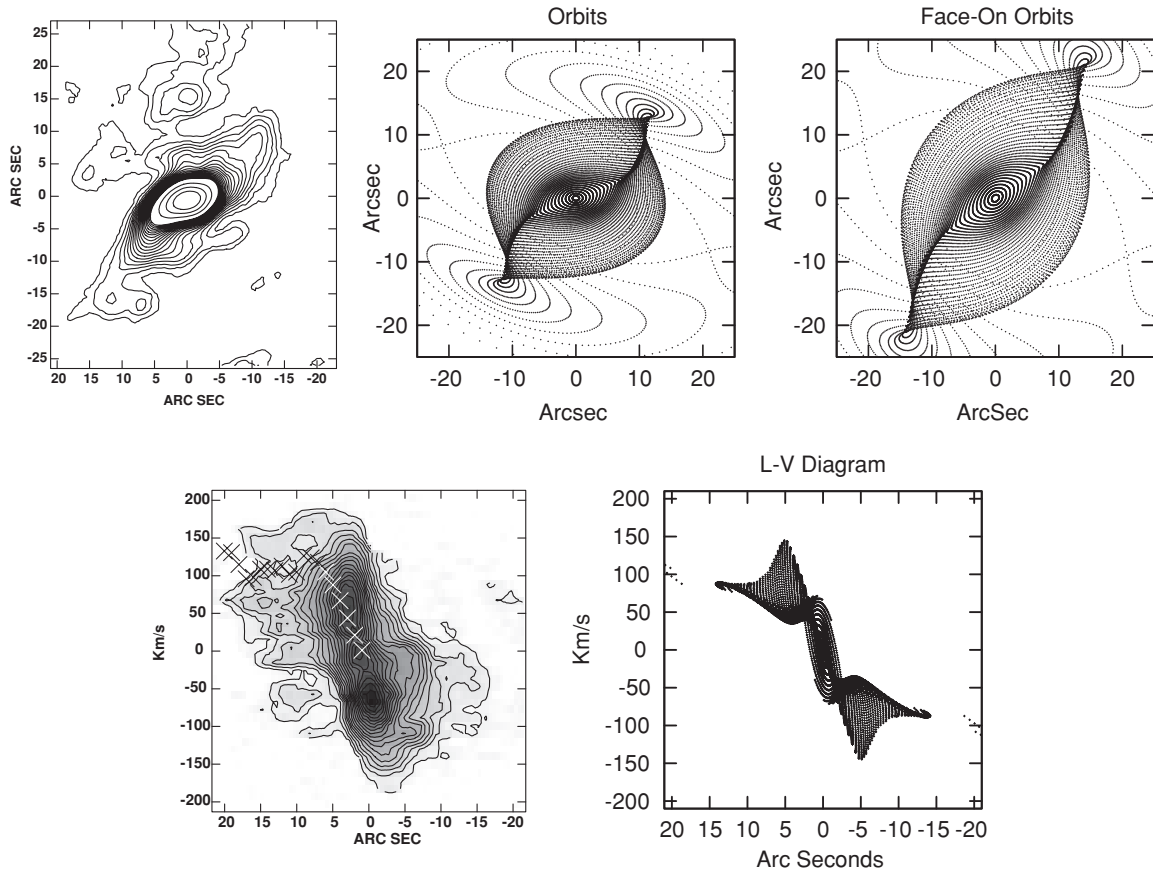


**Figure 9.** Epicyclic weak-bar analytical model for IRAS 04296. Upper left: the CO(1–0) map (see Figure 7). Upper center: the corresponding model for the morphology of the gas. Regions of high dot concentration reflect the expected locations of gas-populated orbits. Upper right: the same model de-inclined to show the face-on morphology of the bar. Lower left: the position–velocity (PV) diagram taken along the major axis (see Table 1) of the galaxy, uncorrected for inclination. The zero velocity coordinate in the figure corresponds to  $2079 \text{ km s}^{-1}$  and the zero position coordinate corresponds to  $\alpha(\text{J2000}) = 04^{\text{h}}32^{\text{m}}48^{\text{s}}.56$ ;  $\delta(\text{J2000}) = 29^{\circ}29'57''.6$ . Crosses mark the fitted azimuthally averaged rotation curve. Uncertainties are given by the size of the symbol, except for the points at the largest radii, which have significantly higher uncertainties. Lower right: the PV diagram for the model, generated in a consistent fashion for comparison with the observed PV diagram.

fidelity (e.g., Lindblad & Lindblad 1994). The current model is that of Sakamoto et al. (1999), except that we use an axisymmetric potential that generates a Brandt rotation curve. With the analytical model we can quickly search barred galaxy parameter space for configurations consistent with what is observed.

Figure 9, which shows the bar models and rotation curve, indicates a close agreement of models with the observed morphology and kinematics. From the best models we find that the molecular gas distribution of IRAS 04296 is very well reproduced by a large axial ratio bar. We assume that the northern portion of the galaxy is the near side, consistent with two fairly straight trailing arms on the leading edge of the bar. The observed velocity residuals have the expected signatures of inflow along the downstream sides of the bar arms and weaker outflow on the upstream (so-called spray region) sides of the arms. Both modeled radial velocities and peak observed velocity residuals are in the range of  $V_r \sim 10 - 40 \text{ km s}^{-1}$ .

#### 4. DISCUSSION

##### 4.1. The Star Formation Rate and Luminosity of the Starburst in IRAS 04296

From the observed free–free emission (Section 3.2) we can infer the Lyman continuum rate of the starburst, its  $L_{\text{IR}}$ , and star formation rate (SFR). The compact centimeter-wave

emission of IRAS 04296 consists of an east–west elongated source, centered at R.A. =  $04^{\text{h}}32^{\text{m}}48^{\text{s}}.6$ , decl. =  $29^{\circ}29'57''$ . The brightest emission corresponds to a region  $0'.4 \times 0'.2$  in size ( $50 \text{ pc} \times 30 \text{ pc}$ ) with a flux of  $\sim 3 \text{ mJy}$  and a flat spectrum, located about  $1''$  ( $140 \text{ pc}$ ) WSW of the dynamical center. There is a halo of emission, stronger to the south of the double source (Figure 3). The emission measure, EM, of these H II regions is high; our high-resolution maps (Figures 5 and 6) detect only gas with  $\text{EM} > 10^6 - 10^7 \text{ cm}^{-6} \text{ pc}$ , which is characteristic of dense or compact H II regions in the Galaxy. The central double radio source has a total flux  $\sim 7 \text{ mJy}$  at  $1.3 \text{ cm}$ , and  $\sim 10 \text{ mJy}$  at  $2$  and  $3.6 \text{ cm}$ . The short wavelength ( $2 - 0.26 \text{ cm}$ ) continuum emission is consistent with star formation having a free–free flux of  $\sim 5 - 7 \text{ mJy}$ , which implies an ionizing flux from young stars of  $\dot{N}_{\text{Ly}\alpha} \sim 6 \pm 2 \times 10^{53} \text{ s}^{-1}$  for optically thin emission. This total Lyman continuum rate is equivalent to  $1.4 \pm 1 \times 10^5 \text{ O7}$  (Martins et al. 2005) stars. Using STARBURST99 (Leitherer et al. 1999; Vázquez & Leitherer 2005) and a Kroupa initial mass function (IMF) with mass cutoffs of  $0.1$  and  $100 M_{\odot}$ , we infer a luminosity associated with the OB stars of  $L_{\text{OB}} \sim 2 \pm 0.7 \times 10^{10} L_{\odot}$  for the nuclear ( $R < 150 \text{ pc}$ ) starburst, to within a factor of 2, given uncertainties in free–free flux and starburst age. The mid-IR continuum flux gives a consistent picture: the  $12 \mu\text{m}/\text{radio}$  flux ratio of 100 is similar to the values of 50–100 observed in both Galactic and extragalactic H II regions (e.g., Genzel et al. 1982; Ho et al. 1989). The thermal

centimeter-wave fluxes imply an SFR of  $\sim 12 \pm 6 M_{\odot} \text{ yr}^{-1}$  and a mass of  $2 \pm 1 \times 10^7 M_{\odot}$  for the nuclear starburst. From the morphology, we infer that these are two massive young super star clusters, “hyper star clusters,” each containing 50,000 O stars and with individual masses of  $\sim 10^7 M_{\odot}$ . The nuclear starburst contains about half of the current global SFR of IRAS 04296, based on the ratio of LWS flux for the nuclear source to the IRAS 12  $\mu\text{m}$  flux for the entire galaxy.

#### 4.2. A Super CO-rich Galaxy: Conversion Factors and Estimating IRAS 04296's $H_2$ Mass

IRAS 04296 is very bright in CO. Its total mapped CO luminosity is  $L_{\text{CO}} = 1.4 \times 10^9 \text{ K km s}^{-1} \text{ pc}^2$ . The nucleus is the dominant feature in the CO maps. The peak integrated CO(1–0) intensity averaged over the central kpc ( $R = 3''.5$ ) is higher than the peak CO brightness averaged over individual giant molecular cloud (GMC) scales in the nearby gas-rich spiral, IC 342 (e.g., Meier et al. 2000). Among nearby galaxies, only NGC 2146, also an LIRG, and possibly NGC 253, can rival it in the richness of its molecular emission (Jackson & Ho 1988; Young et al. 1988).

The bright CO implies a large  $H_2$  mass. For a Galactic conversion factor of  $X_{\text{CO}}^{\text{gal}} = 2 \times 10^{20} \text{ cm}^{-2} (\text{K km s}^{-1})^{-1}$  (e.g., Strong et al. 1988; Hunter et al. 1997), we would derive a molecular gas total mass of  $M_{\text{H}_2}(R < 500 \text{ pc}) = 1.6 \times 10^9 M_{\odot}$  for the central kpc, which is larger than the molecular mass of the entire Milky Way. This mass is comparable to the dynamical mass for the central kpc, as determined by the rotation curve from our model (Figure 9). Either molecular gas accounts for the entirety of the dynamical mass in the inner 500 pc radius or the CO-to- $H_2$  conversion factor is different than in the Galaxy. Evidence is accumulating that the latter explanation is far more likely in the center of a gas-rich galaxy such as IRAS 04296. Studies of a variety of galaxies indicate that  $X_{\text{CO}}^{\text{gal}}$  as determined from the molecular clouds in the disk of our Galaxy is inappropriate for the central regions of galaxies. In (U)LIRGs, it is well known that the Galactic conversion factor consistently overestimates (nuclear) molecular masses by factors of 3–4 (e.g., Downes et al. 1993; Solomon et al. 1997; Yao et al. 2003; Narayanan et al. 2005). This is often called the “starburst” conversion factor. However, in fact, this lower conversion factor also holds in gas-rich centers of normal spiral galaxies including relatively quiescent ones such as our own (e.g., Mauersberger et al. 1996; Dahmen et al. 1998; Meier & Turner 2001, 2004; Weiss et al. 2001; Paglione et al. 2001; Meier et al. 2008). Since  $X_{\text{CO}}$  is a dynamical measure of mass, any contribution to the cloud line widths from systematic motions driven by the stellar potential will cause an overestimate of the gas mass. This is particularly likely in galactic centers, where tidal effects on the clouds become important (e.g., Meier & Turner 2004).

Our  $^{13}\text{CO}$  map provides an independent measure of gas mass, which we can obtain from this optically thin line by “counting molecules.” If we adopt abundances of  $[^{12}\text{CO}/^{13}\text{CO}] = 60$ , (e.g., Wilson & Rood 1994), and  $[^{12}\text{CO}/H_2] = 8.5 \times 10^{-5}$  (Frerking et al. 1982), and an excitation temperature,  $T_{\text{ex}} = 20 \text{ K}$ , which are typical of clouds in the nuclei of nearby galaxies, then  $N(H_2)$  column densities can be estimated from  $^{13}\text{CO}$  line strengths. The peak nuclear column densities derived from  $^{13}\text{CO}$  are 3.6 times lower than the corresponding values obtained from  $^{12}\text{CO}$  using the Galactic  $X_{\text{CO}}$ . Our  $^{13}\text{CO}$  mass suggests that  $X_{\text{CO}}^{\text{nuc}} \simeq 0.6 \times 10^{20} \text{ cm}^{-2} (\text{K km s}^{-1})^{-1}$  in IRAS 04296,

similar to values found for other spiral nuclei, LIRGs, and ULIRGs.

We conclude that the nuclear  $H_2$  mass (including He) for IRAS 04296 is  $M_{\text{H}_2}(R < 500 \text{ pc}) \simeq 4.3 \times 10^8 M_{\odot}$  ( $\Sigma_{\text{H}_2} \simeq 600 M_{\odot} \text{ pc}^{-2}$ ) for the inner kpc, with estimated uncertainties of  $\sim 50\%$  due to unknown  $^{13}\text{CO}$  excitation temperature and abundance. Caution should be used in comparing this value to masses determined for other galactic centers in the literature in which the Galactic  $X_{\text{CO}}$  is used to determine the mass; those masses are probably systematically overestimated.

Outside the nucleus, the CO intensity in the disk remains high in absolute terms. Normalized by distance squared, the CO intensity of IRAS 04296 averaged over its central  $45''$  aperture is larger than any galaxy observed in the FCRAO survey (Young et al. 1995) out to its 30 Mpc distance. Over the central arcminute of the OVRO field of view a total of  $M_{\text{gas}}(R < 30'') = 6 \times 10^9 M_{\odot}$  of molecular gas is implied (for a Galactic conversion factor including He). Even adopting the lower M82 conversion factor (Walter et al. 2002) for this rather normal appearing disk, IRAS 04296 has twice the molecular mass of M82, including all outflows and streamers.  $^{13}\text{CO}(1-0)$  is weakly detected toward the disk in IRAS 04296, so further constraints on the validity of the conversion factor are testable here as well. At  $10''$  radii, the values of  $N(H_2)$  derived from  $^{13}\text{CO}$  are within a factor of 1.6 of what the standard conversion factor predicts, and along the arms at distances larger than  $10''$  (particularly at the bar ends), the two column densities agree within the uncertainties. This suggests that  $X_{\text{CO}}$  in the disk of IRAS 04296 may be consistent with Galactic disk values. However, gradients in excitation temperature,  $^{13}\text{CO}$  opacity, and isotopic abundances can affect the  $^{13}\text{CO}$  mass by at least a factor of 2, so this merits further study.

The IR luminosity of IRAS 04296 is  $\sim 9.8 \times 10^{10} L_{\odot}$  (Sanders et al. 2003). Averaged over the central arcminute, IRAS 04296 has  $L_{\text{IR}}/L_{\text{CO}} = 72 L_{\odot} (\text{K km s}^{-1} \text{ pc}^2)^{-1}$ ,  $L_{\text{IR}}/M_{\text{H}_2} = 18 L_{\odot}/M_{\odot}$ , and  $M(H_2/M_{\text{HI}}) \gtrsim 5$ , all typical of LIRGs (e.g., Scoville et al. 1991; Sanders & Mirabel 1996). Given the rotation curve (Section 3), an inclination of  $50^\circ$  and the molecular gas masses derived above, molecular gas accounts for at least 30% of the dynamical mass within the central 500 pc radius (using the lower  $^{13}\text{CO}$  mass) and 15% of the dynamical mass over the entire mapped region.

#### 4.3. Gas Stability Against in the Molecular Bar

Is the molecular gas disk in IRAS 04296 so dense that it will collapse into new stars without further triggering, or is the disk stable? We can assess this using the Toomre  $Q$  parameter

$$Q = \frac{\alpha \kappa \sigma}{\pi G \Sigma_{\text{gas}}} = \frac{\Sigma_{\text{crit}}}{\Sigma_{\text{gas}}}, \quad (1)$$

where  $\kappa$  is the epicyclic frequency (e.g., Binney & Tremaine 1987),  $\sigma$  is the gas velocity dispersion,  $\Sigma_{\text{gas}}$  is the total gas surface density, and  $\alpha$  is a constant of order unity depending on the structure of the galactic disk (here assumed to be  $\alpha = 1$ ; Safronov 1960; Toomre 1964). If  $Q \lesssim 1$  the gas disk is unstable.

Figure 10 displays the observed values of  $\Sigma_{\text{gas}}$  (calculated both from  $^{12}\text{CO}$  and  $^{13}\text{CO}$ , neglecting the H I surface density contribution, which if conservatively estimated to be distributed uniformly over the disk contributes much less than 10% everywhere within  $R = 17''.5$ ),  $\sigma$ ,  $\kappa$ , and  $Q$  as a function of galactocentric radius. The data have been averaged in azimuth assuming a disk inclined at  $50^\circ$  to the line of sight. For  $^{12}\text{CO}$  and the

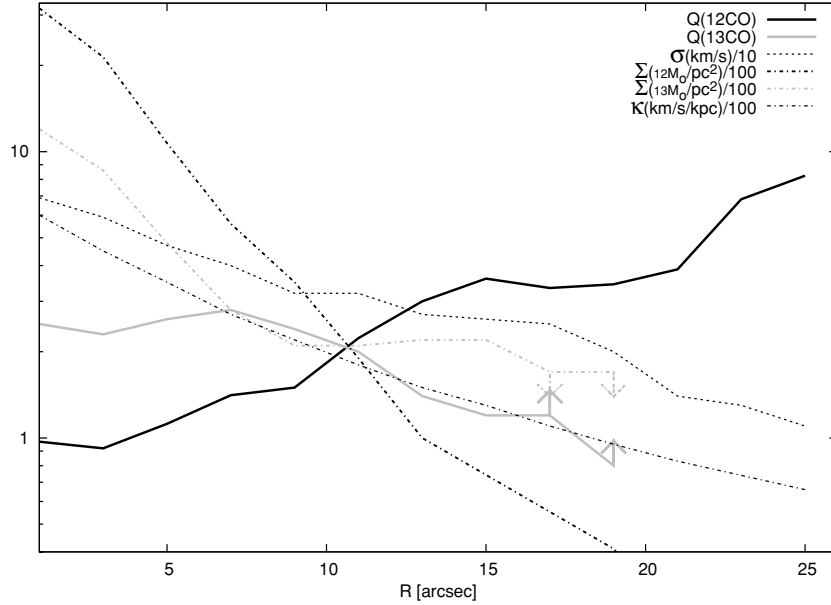


**Figure 10.** Surface densities and Toomre  $Q$  parameters for IRAS 04296. The dot-dashed lines are the azimuthally average molecular surface densities,  $\Sigma_{\text{H}_2}$ , as a function for galactocentric radius. Black lines correspond to  $\Sigma_{\text{gas}}$  calculated using CO(1–0) and the Galactic CO-to- $\text{H}_2$  conversion factor, while gray lines correspond to  $\Sigma_{\text{gas}}$  calculated from  $^{13}\text{CO}(1-0)$  assuming it is optically thin (Section 3.3), both inclination corrected. The velocity dispersion  $\sigma$  (dashed line) is taken from the line width of the CO(1–0) transition, and  $\kappa$  (dotted line) from the fitted rotation curve (Section 3). The resulting Toomre  $Q$  parameter (Section 4.3) is displayed as the thick solid line (black for values from CO determined surface densities and gray for  $^{13}\text{CO}$  gas surface density determinations). Units and scaling for the vertical axis are given in the figure legend.

Galactic conversion factor,  $Q \simeq 1$  for the inner  $5''$  and rises to 3–4 by the end of the bar. This dependence is driven primarily by the rapid drop in gas surface density just outside the nucleus together with the fact the velocity dispersion of the gas remains fairly large ( $\sigma \simeq 20\text{--}40 \text{ km s}^{-1}$ ) along the entire molecular bar. At first glance, this is consistent with gravitational instabilities driving the starburst. But note that this depends on the overestimated  $\text{H}_2$  mass from the standard conversion factor. If we use  $\Sigma_{\text{gas}}$  derived from optically thin  $^{13}\text{CO}$  emission, a rather different picture appears. In this case, derived  $Q$ s would be effectively constant with radius over much of the bar and the disk would be stable everywhere. This suggests that the starburst is not a result of gravitational instabilities in a disk alone and possibly that the large shear/non-circular motions in the strong bar act to inhibit star formation in the arms. The morphology of CO and the starburst’s location at the inner terminus of the bar (Figure 8) argue for bar induced cloud–cloud collisions as inflowing molecular gas piles up in the nucleus.

## 5. ENHANCED STAR FORMATION EFFICIENCY IN THE NUCLEUS

From the nuclear mass and disk mass determinations, and the SFRs, we can compare nuclear and disk star formation efficiencies (SFEs). We consider three representations of SFE: (1) the gas consumption timescale,  $\tau_{\text{SF}} = (\Sigma_{\text{gas}}/\Sigma_{\text{SFR}})$ , (2) the ratio of the mass of formed stars to total mass available in stars + gas,  $\eta = [M_{\text{stars}}/(M_{\text{gas}} + M_{\text{stars}})]$ , and (3)  $L_{\text{IR}}/M_{\text{gas}}$ .

We obtain the SFR for disk ( $0.5 \text{ kpc} < R < 4.3 \text{ kpc}$ , not inclination corrected) and nucleus ( $R < 500 \text{ pc}$ ) in different ways. We estimate the nuclear SFR from our free-free fluxes for the inner  $5''$  region, as described in Section 4.1 (which are also consistent with the  $11.7\mu\text{m}$  LWS flux). We obtained  $N_{\text{Lyc}}^{\text{nuc}} = 6 \pm 1 \times 10^{53} \text{ s}^{-1}$ , equivalent to  $L_{\text{OB}}^{\text{nuc}} = 2 \times 10^{10} L_{\odot}$ , or a total stellar mass associated with the young stars of

$M_{\text{stars}}^{\text{nuc}} = 2 \times 10^7 M_{\odot}$ , and an estimated  $\text{SFR}^{\text{nuc}} = 12 M_{\odot} \text{ yr}^{-1}$ . For the disk SFR, we cannot use our radio continuum maps, since they are not sensitive to extended emission. To estimate the SFR of the disk, we use the *IRAS*  $12 \mu\text{m}$  flux and subtract off the nuclear contribution using our  $11.7 \mu\text{m}$  LWS flux. About half of the *IRAS*  $12 \mu\text{m}$  flux originates from the inner  $5''$  of IRAS 04296. The total disk SFR is only slightly higher than that of the nuclear starburst, at  $\text{SFR}^{\text{disk}} \sim 13 \pm 5 M_{\odot} \text{ yr}^{-1}$ , or 2–5 times that of the Milky Way. The total predicted luminosity in massive stars (if we assume the  $12 \mu\text{m}$  flux is excited by OB stars) produces only half of the observed total infrared luminosity, which will also have contributions from both older populations of stars and regions of exclusively low-mass star formation. Our SFR value for the disk may therefore be an underestimate of the true SFR, but only significantly so if the predominant mode of star formation is exclusively low mass, which we view as unlikely.

To determine the nuclear SFE, we use the nuclear gas mass (from  $^{13}\text{CO}$  including He)  $M_{\text{gas}}^{\text{nuc}} = 4.3 \times 10^8 M_{\odot}$ . The nuclear SFE can then be represented as  $(L_{\text{IR}}/M_{\text{gas}})^{\text{nuc}} \sim (L_{\text{OB}}/M_{\text{gas}})^{\text{nuc}} \sim 30\text{--}50$ , with the uncertainty due to the gas mass. This is high, but within the range found for starburst galaxies (Young & Scoville 1991). The surface density of star formation for this region is then  $\Sigma_{\text{SFR}}^{\text{nuc}}(R < 500 \text{ pc}) = 15 \pm 9 M_{\odot} \text{ yr}^{-1} \text{ kpc}^{-2}$ . The surface density of gas, which we assume is all molecular, is  $\Sigma_{\text{gas}}(R < 500 \text{ pc}) = 600 M_{\odot} \text{ pc}^{-2}$ . This SFE point lies about an order of magnitude above the nominal relation for the Kennicutt–Schmidt law (Kennicutt 1998), although within the scatter. The gas depletion timescale,  $\tau_{\text{SF}}^{\text{nuc}} = 4 \times 10^7 \text{ yr}$ , 50 times shorter than the disk value of  $\tau_{\text{SF}} = 2 \text{ Gyr}$  found for the 23 local spiral galaxies of the THINGS survey (Leroy et al. 2008) and more than 20 times shorter than the  $\tau_{\text{SF}} \sim 1 \text{ Gyr}$  in M51 (Kennicutt et al. 2007; Blanc et al. 2009) at similar gas surface densities. In terms of the percentage of molecular mass converted to stars,  $\eta^{\text{nuc}} \simeq 5\% \pm 1\%$  over the 500 pc of our CO beam, and is almost certainly significantly

higher on smaller GMC scales. This SFE is already somewhat high for GMC scales of 50 pc or more, but is characteristic of SFEs seen in the Galaxy on cluster (<10 pc) scales (e.g., Lada & Lada 2003). Therefore, star formation appears to progress at an elevated, but not unusual efficiency in the nucleus.

From the SFR and molecular gas mass estimated for the disk, we can compute the disk SFE. Using the Galactic value of the CO–H<sub>2</sub> conversion factor appropriate for disks, we compute a disk-only molecular gas mass of  $M_{\text{H}_2}^{\text{disk}} = 4.3 \times 10^9 M_{\odot}$ , which is 10 times the mass of the nuclear gas. The SFR over the entire disk, by contrast, is comparable to that of the nucleus, at  $\text{SFR}^{\text{disk}} \sim 13 \pm 5 M_{\odot} \text{yr}^{-1}$ . We find  $(L_{\text{IR}}/M_{\text{gas}})^{\text{disk}} \sim (L_{\text{OB}}/M_{\text{gas}})^{\text{disk}} \sim 5$ , uncertain to about a factor of 2 largely due to gas mass. This is similar, within the uncertainties, to the global Galactic value of 8 (Young & Scoville 1991, corrected to our value of  $X_{\text{CO}}^{\text{Gal}}$ ). The surface density of star formation is then  $\Sigma_{\text{SFR}}^{\text{disk}} \sim 0.3 \pm 0.15 M_{\odot} \text{yr}^{-1} \text{kpc}^{-2}$ . The surface density of gas, which we assume is all molecular in this region, is  $\Sigma_{\text{gas}}^{\text{disk}} = 75 M_{\odot} \text{pc}^{-2}$ . The disk SFE can also be represented by  $\Sigma_{\text{SFR}}/\Sigma_{\text{gas}}^{\text{disk}} = 3.0 \times 10^{-9} \text{yr}^{-1}$ , or a gas consumption timescale of  $\tau_{\text{SF}}^{\text{disk}} \sim 3.3 \times 10^8 \text{yr}$ . The gas consumption timescale is a factor of 6 shorter than the typical THINGS galaxy (Leroy et al. 2008), and a factor of 3 shorter than the average value for M51 (Blanc et al. 2009). In terms of percentage of molecular gas converted into stars,  $\eta^{\text{disk}} = 0.5\%$ . Within the uncertainties, this is consistent with the SFE of  $\sim 1\%$  observed for Galactic disk star formation on GMC scales (Lada & Lada 2003; Ikeda et al. 2007; Higuchi et al. 2009; Johnston et al. 2009).

A low disk SFE is consistent with the model of a nuclear starburst produced through secular evolution. If nuclear star formation is seen, it means that fresh gas must be present in the nucleus, else it would have formed stars long ago. In a morphologically undisturbed galaxy such as IRAS 04296, the nuclear gas must be a product of secular evolution. If the SFE of the disk were higher, then the gas would be used up before it arrived in the nucleus. Much of the molecular gas presently lies within 1.7 kpc (12'') of the center. At this radius, the orbital timescale is  $\sim 10^8 \text{yr}$ . If we estimate the velocity for the outermost gas in IRAS 04296 to drift inward via secular evolution to be a few  $\text{km s}^{-1}$  (Section 3.3; Athanassoula 1992; Kormendy & Kennicutt 2004), then the timescale for all of the CO gas in the disk of IRAS 04296 to drift into the nucleus is  $\sim 1 \text{Gyr}$ . The star formation timescale averaged over the disk is  $\tau_{\text{SF}}^{\text{disk}} \sim 3 \times 10^8 \text{yr}$ . If the SFE were much larger than this, then there would be no build-up of nuclear gas, and we would not see strong nuclear star formation.

We conclude that the SFE in the nucleus of IRAS 04296 is an order of magnitude higher than the SFE in its disk. The value  $\eta^{\text{disk}} \sim 0.5\%$ , for the disk of IRAS 04296 is consistent with the Milky Way value of  $\eta \sim 1\%$  on GMC scales. The value of  $\eta^{\text{nuc}} \gtrsim 5\%$  found for the nucleus is consistent with SFE values on cluster (<10 pc) scales in the Galaxy. The corresponding star formation timescales are  $\tau_{\text{SF}}^{\text{nuc}} \sim 3 \times 10^7 \text{yr}$  for the nucleus and  $\tau_{\text{SF}}^{\text{disk}} \sim 3.3 \times 10^8 \text{yr}$  for the disk. While the disk percolates along at normal Galactic disk SFRs, the starburst mode ‘‘waits’’ until the gas has drifted to the nucleus.

## 6. COMPARISON OF IRAS 04296 WITH OTHER NEARBY GALAXIES AND LIRGS

IRAS 04296 is an LIRG of the local universe. We now place IRAS 04296 in the context of the other better-known members of that class: NGC 2146, NGC 7552, NGC 4418, NGC 1365,

and NGC 1068. NGC 1068 and NGC 1365 contain active nuclei which contribute significant fractions of their total luminosity. NGC 7552 hosts a weak LINER. NGC 4418 is thought to be a Seyfert 2 because it contains a very compact bright nucleus (Eales et al. 1990; Evans et al. 2003), but it is no more compact than the infrared continuum from IRAS 04296. NGC 4418 actually resembles a compact nuclear starburst more than the composite galaxies with which it is usually classed. NGC 2146, along with the less luminous galaxies M82 and the Antennae, are thought, like IRAS 04296, to be pure starbursts.

In contrast to NGC 4418 and IRAS 04296, star formation is more spatially extended in the remainder of the LIRGs. NGC 7552 and NGC 1068 have kpc-scale starburst rings, well outside the nucleus. The starburst-dominated galaxies, NGC 2146, NGC 1365, M82, and the Antennae, have starbursts extended over many hundreds of parsecs. NGC 7552 and NGC 1365 are the only other starburst-dominated local LIRGs that do not appear overly disturbed; both have barred stellar appearances similar to IRAS 04296s. NGC 7552 may have experienced a similar dynamical history to IRAS 04296, namely, slow, bar-mediated evolution, although in IRAS 04296’s case the starburst is concentrated in the nucleus, whereas NGC 7552’s enhanced star formation occurs well before the gas reaches the nucleus.

The local universe LIRGs are a surprisingly diverse class. Many of the differences are probably because they are at different evolutionary stages but others appear to be more fundamental. They may perhaps relate to the underlying causes and mechanisms of the starbursts.

## 7. CONCLUSIONS: FIRST LOOK AT IRAS 04296, A BAR-DRIVEN STARBURST TURNING ON

The little-studied nearby (29 Mpc) LIRG, IRAS 04296, is a barred and normal-appearing spiral galaxy, with an intense nuclear starburst and a vast reservoir of molecular gas. Mid-IR and radio continuum imaging show that IRAS 04296 currently has a bright nuclear starburst containing the equivalent of  $\sim 10^5$  O7 stars ( $N_{\text{Lyc}}^{\text{nuc}} \sim 6 \pm 2 \times 10^{53} \text{s}^{-1}$ ). This  $\sim 150 \text{pc}$  region alone has the equivalent of more than half the star-forming luminosity in the entire 500 pc starburst region in M82. The nuclear starburst region accounts for  $\sim 50\%$  of the total current star formation in the galaxy as measured by  $11.7\mu\text{m}$  continuum flux, and contributes  $\sim 20\%$  of the total IRAS luminosity of IRAS 04296. The starburst luminosity is concentrated in a double source that is  $\lesssim 50 \text{pc}$  in size, located near the inner end of the northwestern bar arm. Radio and mid-IR images suggest that these are the H II regions associated with two massive young super star clusters containing a total of  $2 \pm 1 \times 10^7 M_{\odot}$  of stars, and a total young stellar luminosity of  $L_{\text{OB}} = 2 \pm 0.7 \times 10^{10} L_{\odot}$ .

The morphology and kinematics of the CO emission of IRAS 04296 show a starburst that is being fueled by slow gas inflow along a bar. We can estimate the history and lifetime of the starburst from the gas content and inflow velocity. If the velocity of gas inflow to the nuclear starburst is the maximum value of the average observed bar-induced peculiar velocity,  $\sim 20 \text{km s}^{-1}$ , a net radial inflow of gas along the arm width ( $\sim 750 \text{pc}$  at  $10''$ ) of  $9 M_{\odot} \text{yr}^{-1}$  results (for a Galactic conversion factor relevant to the arms). For more expected net inflow rates of a few percent of the orbital velocity (Athanassoula 1992),  $\dot{M}_{\text{inf}} \lesssim 1 M_{\odot} \text{yr}^{-1}$ . The SFR in IRAS 04296 from the thermal radio continuum is consistent with a current, nuclear star formation rate of  $\text{SFR}^{\text{nuc}} \sim 12 \pm 6 M_{\odot} \text{yr}^{-1}$  and as much as

$\text{SFR}^{\text{tot}} \sim 25 \pm 10 M_{\odot} \text{ yr}^{-1}$  total for the galaxy as a whole. The nuclear star formation is not in equilibrium with the net inflow rate and hence the starburst is currently consuming its reservoir of nuclear fuel faster than it is being replenished.

Stellar mass buildup also dictates that the current rate of nuclear star formation is not sustainable over the long term, that it is a true starburst. Subtracting the gas mass from the dynamical mass leaves a small nuclear stellar mass of  $\lesssim 1.2 \times 10^9 M_{\odot}$ . Nuclear star formation also could not have been occurring at the current  $\sim 12 M_{\odot} \text{ yr}^{-1}$  rate for more than the past  $\sim 10^8$  yr or the stellar mass would exceed the observed dynamical mass.

We also find that the SFE is a function of position in the galaxy. We derive a starburst timescale of  $\tau_{\text{SF}}^{\text{nuc}} = 3.7 \times 10^7$  yr for the nucleus ( $R < 500$  pc), or  $\eta^{\text{nuc}} = 5\%$ ; the star formation timescale is 10 times longer in the disk, and the SFE is only  $\eta^{\text{nuc}} = \sim 0.5\%$ . The relatively low SFE observed in the disk, where the gas consumption timescale is  $\sim 5$  orbital times, is necessary so that gas drifting into the nucleus along the bar orbits would not be consumed before it reached the center. Any higher value for the disk SFE would be inconsistent with a nuclear starburst fueled by gas drifting inward via bar inflow.

Taken together these facts imply that we are witnessing an early stage of starburst/bar inflow induced secular evolution in the history of IRAS 04296. Otherwise the bulge would be much larger and the disk would be depleted of its gas.

D.S.M. acknowledges support from the National Radio Astronomy Observatory which is operated by Associated Universities, Inc., under cooperative agreement with the National Science Foundation. The anonymous referee is thanked for a helpful report. The Owens Valley Millimeter Interferometer is operated by Caltech with support from the NSF under grant AST-9981546. This research has made use of the NASA/IPAC Extragalactic Database (NED) which is operated by the Jet Propulsion Laboratory, California Institute of Technology, under contract with the National Aeronautics and Space Administration.

*Facilities:* CMA, Hale (Wide-field Infrared Camera), Keck:I (Long Wavelength Spectrometer), VLA

## REFERENCES

- Armus, L., et al. 2007, *ApJ*, **656**, 148  
 Athanassoula, E. 1992, *MNRAS*, **259**, 345  
 Binney, J., & Tremaine, S. 1987, *Galactic Dynamics* (Princeton, NJ: Princeton Univ. Press), 747  
 Blanc, G. A., Heiderman, A., Gebhardt, K., Evans, N. J., & Adams, J. 2009, *ApJ*, **704**, 842  
 Brandl, B. R., et al. 2004, *ApJS*, **154**, 188  
 Chamaraux, P., Kazes, I., Saito, M., Yamada, T., & Takata, T. 1995, *A&A*, **299**, 347  
 Clemens, M. S., Vega, O., Bressan, A., Granato, G. L., Silva, L., & Panuzzo, P. 2008, *A&A*, **477**, 95  
 Condon, J. J. 1992, *ARA&A*, **30**, 575  
 Condon, J. J., Helou, G., Sanders, D. B., & Soifer, B. T. 1996, *ApJS*, **103**, 81  
 Condon, J. J., Huang, Z.-P., Yin, Q. F., & Thuan, T. X. 1991, *ApJ*, **378**, 65  
 Dahmen, G., Hüttemeister, S., Wilson, T. L., & Mauersberger, R. 1998, *A&A*, **331**, 959  
 Downes, D., & Solomon, P. M. 1998, *ApJ*, **507**, 615  
 Downes, D., Solomon, P. M., & Radford, S. J. E. 1993, *ApJ*, **414**, L13  
 Eales, S. A., Becklin, E. E., Hodapp, K.-W., Simons, D. A., & Wynn-Williams, C. G. 1990, *ApJ*, **365**, 478  
 Evans, A. S., et al. 2003, *AJ*, **125**, 2341  
 Frerking, M. A., Langer, W. D., & Wilson, R. W. 1982, *ApJ*, **262**, 59  
 Genzel, R., Becklin, E. E., Moran, J. M., Reid, M. J., Jaffe, D. T., Downes, D., & Wynn-Williams, C. G. 1982, *ApJ*, **255**, 527  
 Genzel, R., et al. 1998, *ApJ*, **498**, 579  
 Higuchi, A. E., Kurono, Y., Saito, M., & Kawabe, R. 2009, *ApJ*, **705**, 468  
 Ho, P. T. P., Turner, J. L., Fazio, G. G., & Willner, S. P. 1989, *ApJ*, **344**, 135  
 Hunter, S. D., et al. 1997, *ApJ*, **481**, 205  
 Ikeda, N., Sunada, K., & Kitamura, Y. 2007, *ApJ*, **665**, 1194  
 Jackson, J. M., & Ho, P. T. P. 1988, *ApJ*, **324**, L5  
 Johnston, K. G., Shepherd, D. S., Aguirre, J. E., Dunham, M. K., Rosolowsky, E., & Wood, K. 2009, *ApJ*, **707**, 283  
 Joseph, R. D., & Wright, G. S. 1985, *MNRAS*, **214**, 87  
 Kennicutt, R. C., Jr. 1998, *ApJ*, **498**, 541  
 Kennicutt, R. C., Jr., et al. 2007, *ApJ*, **671**, 333  
 Kormendy, J., & Kennicutt, R. C., Jr. 2004, *ARA&A*, **42**, 603  
 Lada, C. J., & Lada, E. A. 2003, *ARA&A*, **41**, 57  
 Leitherer, C., et al. 1999, *ApJS*, **123**, 3  
 Leroy, A. K., Walter, F., Brinks, E., Bigiel, F., de Blok, W. J. G., Madore, B., & Thornley, M. D. 2008, *AJ*, **136**, 2782  
 Lindblad, P. O., & Lindblad, P. A. B. 1994, in *ASP Conf. Ser. 66, Physics of the Gaseous and Stellar Disks of the Galaxy*, ed. I. R. King (San Francisco, CA: ASP), 29  
 Lutz, D., Spoon, H. W. W., Rigopoulou, D., Moorwood, A. F. M., & Genzel, R. 1998, *ApJ*, **505**, L103  
 Martins, F., Schaerer, D., & Hillier, D. J. 2005, *A&A*, **436**, 1049  
 Mauersberger, R., Henkel, C., Wielebinski, R., Wiklind, T., & Reuter, H.-P. 1996, *A&A*, **305**, 421  
 Meier, D. S., & Turner, J. L. 2001, *ApJ*, **551**, 687  
 Meier, D. S., & Turner, J. L. 2004, *AJ*, **127**, 2069  
 Meier, D. S., Turner, J. L., & Hurt, R. L. 2000, *ApJ*, **531**, 200  
 Meier, D. S., Turner, J. L., & Hurt, R. L. 2008, *ApJ*, **675**, 281  
 Narayanan, D., Groppi, C. E., Kulesa, C. A., & Walker, C. K. 2005, *ApJ*, **630**, 269  
 Paglione, T. A. D., et al. 2001, *ApJS*, **135**, 183  
 Sazonov, V. S. 1960, *Ann. Astrophys.*, **23**, 979  
 Sakamoto, K., Okumura, S. K., Ishizuki, S., & Scoville, N. Z. 1999, *ApJS*, **124**, 403  
 Sanders, D. B., Mazzarella, J. M., Kim, D.-C., Surace, J. A., & Soifer, B. T. 2003, *AJ*, **126**, 1607  
 Sanders, D. B., & Mirabel, I. F. 1996, *ARA&A*, **34**, 749  
 Sanders, D. B., Soifer, B. T., Elias, J. H., Madore, B. F., Matthews, K., Neugebauer, G., & Scoville, N. Z. 1988, *ApJ*, **325**, 74  
 Scoville, N. Z., Carlstrom, J., Padin, S., Sargent, A., Scott, S., & Woody, D. 1994, in *ASP Conf. Ser. 59, IAU Colloq. 140, Astronomy with Millimeter and Submillimeter Wave Interferometry*, ed. M. Ishiguro & J. Welch (San Francisco, CA: ASP), 10  
 Scoville, N. Z., Sargent, A. I., Sanders, D. B., & Soifer, B. T. 1991, *ApJ*, **365**, L5  
 Soifer, B. T., Sanders, D. B., Madore, B. F., Neugebauer, G., Danielson, G. E., Elias, J. H., Lonsdale, C. J., & Rice, W. L. 1987, *ApJ*, **320**, 238  
 Solomon, P. M., Downes, D., & Radford, S. J. E. 1992, *ApJ*, **387**, L55  
 Solomon, P. M., Downes, D., Radford, S. J. E., & Barrett, J. W. 1997, *ApJ*, **478**, 144  
 Strauss, M. A., Huchra, J. P., Davis, M., Yahil, A., Fisher, K. B., & Tonry, J. 1992, *ApJS*, **83**, 29  
 Strong, A. W., et al. 1988, *A&A*, **207**, 1  
 Toomre, A. 1964, *ApJ*, **139**, 1217  
 Turner, J. L., & Ho, P. T. P. 1994, *ApJ*, **421**, 122  
 Vázquez, G. A., & Leitherer, C. 2005, *ApJ*, **621**, 695  
 Wada, K. 1994, *PASJ*, **46**, 165  
 Walter, F., Weiss, A., & Scoville, N. 2002, *ApJ*, **580**, L21  
 Weiss, A., Neininger, N., Hüttemeister, S., & Klein, U. 2001, *A&A*, **365**, 571  
 Wielebinski, R. 1998, *A&A*, **339**, 737  
 Wilson, T. L., & Rood, R. 1994, *ARA&A*, **32**, 191  
 Wilson, J. C., et al. 2003, *Proc. SPIE*, **4841**, 451  
 Yao, L., Seaquist, E. R., Kuno, N., & Dunne, L. 2003, *ApJ*, **588**, 771  
 Young, J. S., Claussen, M. J., Kleinmann, S. G., Rubin, V. C., & Scoville, N. 1988, *ApJ*, **331**, L81  
 Young, J. S., & Scoville, N. Z. 1991, *ARA&A*, **29**, 581  
 Young, J. S., et al. 1995, *ApJS*, **98**, 219